Materials Chemistry and Physics 295 (2023) 126959

Contents lists available at ScienceDirect

Materials Chemistry and Physics

journal homepage: www.elsevier.com/locate/matchemphys

Microstructure and biodegradation performance of Mg–4Ca–1Zn based alloys after ultrasonic treatment and doping with nanodiamonds for biomedical applications

Ekaterina Marchenko [a], Gulsharat Baigonakova [a], Anton Khrustalev [a], Ilya Zhukov [a], Aleksandr Vorozhtsov [a], Timofey Chekalkin [a,b], Aleksandr Monogenov [a], Aleksandr Garin [a], Tae-Woo Kim [c], Seung-Baik Kang [c,*]

[a] National Research Tomsk State University, Tomsk, Russia
[b] R&D Center, TiNiKo Co., Osong, South Korea
[c] SMG-SNU Boramae Medical Center, Seoul National University College of Medicine, Seoul, South Korea

ARTICLE INFO

Keywords:
Mg-based alloys
Biodegradation
Ultrasonic treatment
Nanodiamonds
Topology
Surface potential

ABSTRACT

This work aims to study microstructural features, phase composition, topology, surface potential, and the biodegradation performance of Mg–4Zn–1Ca-based alloys whose melts were ultrasonically (US) treated and doped with nanodiamonds (ND). The findings show a correlation between the ratio of the secondary phase segregated along the grain boundaries and the biodegradation rate in the RPMI-1640 synthetic culture medium. The fewer $Ca_2Mg_6Zn_3$ phase fraction, the lower the biodegradation rate. Also, ND doping does not significantly affect the biodegradation rate. Intriguingly, the latter in the US-treated alloy was found to be noticeably inhibited due to a smoother topography and the presence of the fewest $Ca_2Mg_6Zn_3$ phase fraction segregated along the grain boundaries. Further studies are needed to assess the biodegradable potential of the ND doped alloy, which melt was ultrasonically treated.

1. Introduction

Implants made of biodegradable alloys are among the attractive candidates for trauma and orthopedic surgeries. Using these materials eliminates the need for re-surgery to remove implanted devices after bone tissue healing.

Magnesium and its alloys are fascinating and promising biomaterials for their use as biodegradable implants. Their main advantages are pretty good biocompatibility, mechanical characteristics similar to those shown by bone tissue, and the ability to be dissolved in physiological media. Biodegradable magnesium alloys have been extensively studied for their noted bioresorptive potential compared to traditional bioinert metals. However, in its chemically pure incarnation, the main drawback of Mg-based alloys is an excessive degradation rate, leading to a rapid loss of mechanical integrity before osteogenesis has been finished. In addition, corrosion is accompanied by an extraordinary gaseous reaction in vivo, which negatively affects the host tissues and interferes with the recovery processes [1].

Given the above, designing and studying various biodegradable Mg-based alloys for biomedical applications are very pertinent. Alloying, thermo-mechanical processing, and coating can reduce the biodegradation rate in vivo due to the modified microstructure evident through grain size changing, lesser porosity, formation of intermetallic constituents and secondary phases, presence of a protective surface layer [2–5]. Also, surface modifications are a typical method for improving corrosion resistance, which conceals the material without changing its microstructure [6,7]. In turn, alloying mainly improves mechanical properties such as yield strength, ductility, and corrosion resistance [8,9].

Due to adjustable mechanical properties and variable biodegradation rates, tailored Mg-based alloys with embedded bioactive reinforcing elements can be considered a new generation of implanted devices [10]. So far, a large number of magnesium implants have been suggested for the treatment of bone injuries in humans and animals, including blocks, nails, screws, wires, plates, etc. [11].

Mg alloys are much more plastic than bioceramics, mechanically stronger than biopolymers, and have preferential biodegradation

* Corresponding author.
E-mail address: ossbkang@gmail.com (S.-B. Kang).

https://doi.org/10.1016/j.matchemphys.2022.126959
Received 20 August 2022; Received in revised form 25 October 2022; Accepted 27 October 2022
Available online 31 October 2022

compared to other biomaterials [1,12]. Magnesium is a common mineral existing in the body, playing one of the most crucial roles in bone health, and it can also stimulate and maintain osteogenetic processes [13]. And eventually, Mg is now considered to be the best hope for trauma and orthopedic applications [4].

In the context of a biodegradable material, its predominant constituents should be those that can be metabolized in vivo with appropriate decomposition rates and without releasing of toxic reactants. Mostly, these elements are magnesium, zinc, and calcium [14].

Decomposition products stemming from the electrochemical corrosive reaction of Mg alloys can be excreted through metabolism [15]. Magnesium is known to have mechanical properties similar to those demonstrated by the cortical bone. The elastic modulus of magnesium is 41–45 GPa, with a density of about 1.74 g/cm3, and the yield stress gap varies within 65–100 MPa [16]. While the density of the cortical bone is about 1.8–2.1 g/cm3, the elastic modulus is within 15–25 GPa, and the yield stress is within 130–180 MPa. The mechanical properties of pure magnesium are significantly lower than those of Ti-based alloys for biomedical applications [17], as well as biodegradable Zn- or Mn–Fe--based alloys [18,19].

Zinc is the most abundant and recognized as one of the vital nutrients in the body. Therefore, it is safe and permissible for biomedical applications. Alloying pure magnesium with zinc decreases the biodegradation rate and increases the mechanical properties of resulting Mg-based alloys [18]. The highest value of solute Zn in Mg can reach 6.5 wt%. Solid solution effects on the hardness and flow stress have been studied earlier [20]. A strength increase in alloying with zinc is attributed to solid solution hardening, resulting from the higher shear stress for the basal planes of the Mg crystal lattice. One limiting factor appears to be cracking and micropores upon solidifying of the melt with a Zn-related fraction increase in the alloy.

Calcium is the main structural element of the trabecular bone and plays a crucial role in cellular interactions, sustaining their signaling functions [21]. The solubility level of Ca in Mg is far fewer, reaching about 1.34 wt%. Increasing the ratio leads to the Mg_2Ca phase being segregated along grain boundaries, drastically embrittling the alloy [22]. Alloying with calcium changes the stress-strain behavior due to solid solution and precipitation hardening. Several studies demonstrate that calcium reduces the average grain size of magnesium, which has a beneficial effect on its mechanical properties [23,24].

Some technical modalities, including ultrasonic, vibration, or mechanical treatments, are known to aim at homogenizing and degassing the melt [25,26]. Some papers report that introducing small amounts of nanoparticles increases strength and ductility simultaneously [27]. The high mechanical properties of the diamond allow the use of its nanoparticles as a reliable hardening agent of the matrix, where its small amount contributes to increasing the mechanical performance of alloys [28]. In addition, nanodiamond particles contribute to the higher biocompatibility level of magnesium alloy in contact with living organisms [29].

The ternary Mg–Zn–Ca composition is very encouraging for the current medical industry. Magnesium alloys doped with Zn (3 wt%) and Ca (1 wt%) have been reported to indicate high bioinertness, tolerable mechanical characteristics, and reasonable biodegradation performance [30]. The ultimate strength is 160 MPa with a relative elongation of 8%. The biocorrosion rate in the ternary system decreases gradually in increasing the Zn content up to 3 wt%, followed by a surge occurring in varying the Zn content within 5–9 wt% [31]. Notably, the Mg–4Zn–1Ca alloy indicates low mechanical characteristics, whereas its biodegradation rate seems appropriate for clinical applications [32]. Considering the current data reported in numerous studies, one may infer that issues addressing Mg-based alloys with high mechanical characteristics, showing tailored and controllable biodegradation rates, have come to the fore. Therefore, as we faced with the matters, this study aims to improve the characteristics of the baseline Mg–4Zn–1Ca alloy, customizing it by two suggested routes – (i) ultrasonic treatment of the melt and (ii) doping the melt with diamond nanoparticles. We explored the topography and macro-/microstructure features, together with an assessment of in vitro decomposition potential using the RPMI-1640 synthetic culture medium.

2. Materials and methods

2.1. Alloy preparation

We used pure magnesium (99.9%), metallic zinc (99.9%), and calcium (99.9%) as starting materials. For a comparative assessment, three alloys were prepared as follows:

#1 – baseline Mg–4Zn–1Ca;
#2 – $(Mg–4Zn–1Ca)_{US}$ ultrasonically treated (US);
#3 - $(Mg–4Zn–1Ca)_{ND}$ doped with diamond nanoparticles (ND).

To homogenize the chemical composition of the alloys after cooling, annealing at 300 °C for 6 h was performed, followed by cooling in the furnace.

2.1.1. Alloy # 1 (Mg–4Zn–1Ca)

2 kg of pure magnesium was placed in a steel crucible and melted in the supplied argon flow atmosphere. To melt the alloy, an open-type muffle furnace was used for easy access and controlling the melt. Argon flow was supplied during the entire melting process. Reaching 720 °C, zinc was introduced using a mechanical mixer at a rotation speed of 1200 rpm until complete dissolution, pursuant to the procedure described in Ref. [33]. Afterward, the melt was held at 720 °C using a steel bell method [34] with subsequent calcium addition, using the same mechanical mixer for 20 s, and downpoured into the mold.

2.1.2. Alloy # 2 $(Mg–4Zn–1Ca)_{US}$

The melting procedure was the same as above; however, before downpouring, the melt was ultrasonically treated (US). Ultrasonic treatment was carried out using a magnetostrictive water-cooled transducer with a power of 4.1 kV and a frequency of 17.6 kHz for 60 s.

2.1.3. Alloy # 3 $(Mg–4Zn–1Ca)_{ND}$

Nanodiamonds (ND) depicted in Fig. 1,*a* were obtained by detonation synthesis, as reported by Vorozhtsov et al. [35], and doped with iron, using a planetary mill. The granulometric ND histogram is represented by a unimodal particle size distribution indicated in Fig. 1,*b*. The mean size of spherical-type particles was 7 nm, whereas the min and max size was 1 nm and 18 nm, respectively.

ND were introduced into the melt through an Mg-ND master alloy. ND were mixed with magnesium micropowder (99.9%) in ethanol for 20 min using an ultrasonic bath to obtain a homogenized Mg-5%ND mixture. To obtain a master alloy from a prepared powder mixture, the method of shock-wave compaction was used, as described in Ref. [35].

The Mg-5%ND master alloy was then admixed with the alloy #1 melt at 710 °C, using a mechanical mixer for 60 s, until its complete dissolving. Afterward, the melt was downpoured into a steel mold with the dimensions of 200 × 100 × 10 mm (height × width × thickness). The solidification process of the molten metal was accompanied by simultaneous vibration using a vibrostand, on which the steel mold was securely attached, with a frequency of 60 Hz and an amplitude of 0.5 mm. The schematic view of the melting procedure related to alloy #3 is outlined in Fig. 2.

2.2. Methods

ND were explored using a transmission electron microscope (Philips CM30). The elemental composition of the alloys was investigated using a sequential X-ray fluorescence wave-dispersive spectrometer (Shimadzu XRF-1800). The quantitative phase analysis was performed using an X-

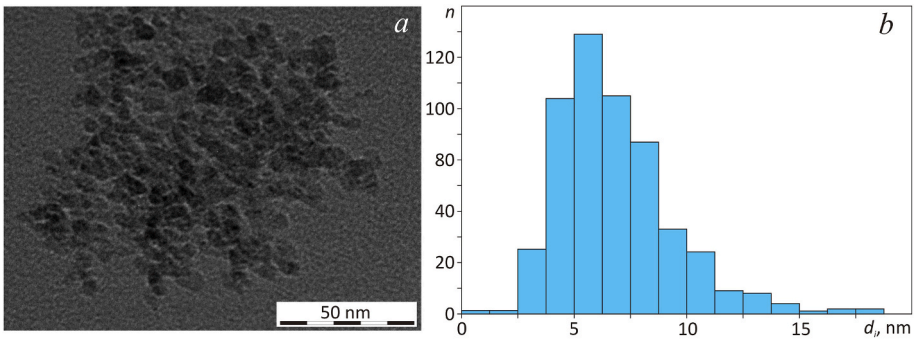

Fig. 1. TEM image (*a*) and granulometric histogram (*b*) of ND.

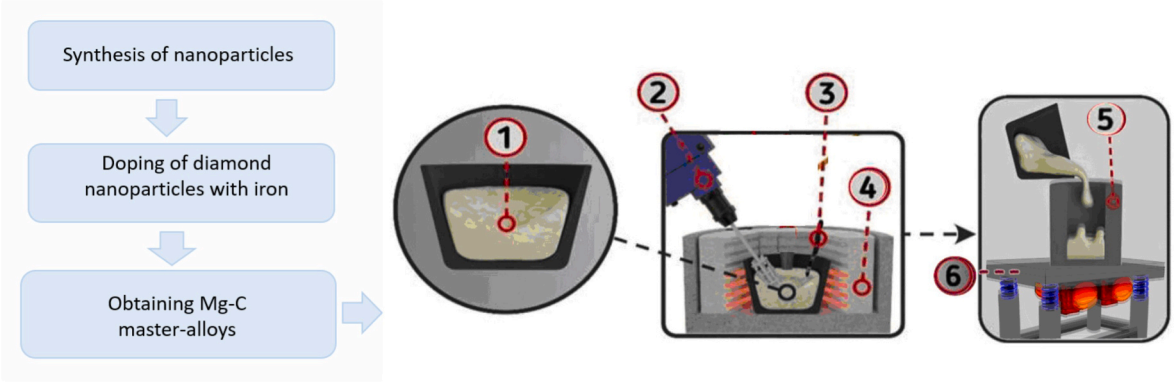

Fig. 2. Schematic view of alloy #3 fabrication route: (1) Mg melt in Ar shielding atmosphere, (2) mechanical mixer, (3) master alloy, (4) furnace, (5) steel mold, and (6) vibrostand.

ray diffractometer with filtered CuK-α radiation (Shimadzu XRD-6000, $2\theta = 20–80^{\circ}$, 10 s exposure).

Metallographic analysis was performed using an optical microscope (Olympus GX71) and a scanning electron microscope (TescanVega II LMU). The structure of the cast materials was studied after standard metallographic grinding followed by polishing without etching. The average grain size was determined by the secant method according to the ASTM 112-13 standard based on at least 600 measurements for each state. The specific area ratio, occupied by the matrix and secondary phases, was analyzed using ImageJ, open-source software for scientific image visualization, processing, and analysis.

Elemental analysis was performed on a Tescan MIRA III LMU, Schottky cathode scanning electron microscope equipped with an Oxford Instruments Ultim Max 40 energy dispersive X-ray spectrometer (Oxford Instruments, High Wycombe, UK). Scanning was performed at an accelerating voltage (HV) of 20 kV.

The topography and electrochemical potential distributions of the sample surface were carried out by atomic force microscopy using an NT-MDT scanning probe microscope with a SOLVER HV vacuum chamber in a semi-contact mode.

To evaluate the biodegradation performance, the prepared cubic samples ($10 \times 10 \times 10$ mm^3) were immersed and dissolved in vitro under simulated conditions similar to aseptic inflammation, which usually occurs after implantation and is accompanied by the accumulation of biological fluids in the host tissue. Prior to the standard immersion test, all samples were dry-heat sterilized at 180 °C for 1 h. To assess the biodegradation rate, samples were immersed in a synthetic culture medium RPMI-1640 with a low content of micronutrients, (g/L) 5.9 NaCl; 0.4 KCl; 0.8 $Na_2P_2O_7$; 0.1 Ca (NO_3); 2.0H_2O, 0.049 $MgSO_4$, 4.5 D-glucose, amino acids and vitamins (Sigma-Aldrich, USA), at 37 °C for a week, using a 6-ml vial for each sample, according to ISO 10993–5. Samples were then taken out in a week and air-dried at 22 °C for two weeks to record the change in sample weight. The mass of the samples was measured using a high-accuracy analytical balance, VM-II (the standard deviation - 0.023 mg).

3. Results

Chemical analysis of the distributed elements indicates the presence of Zn (about 4 wt%) and Ca (about 1 wt%) in all the alloys cast (Table 1). Alloy #2 contains the highest amount of aluminum with the least amount of calcium. This fact may be due to the applied ultrasonic treatment for 60 s, when Ca partially burns out and is trapped by forming slags.

Analyzing X-ray diffraction patterns indicates that all alloys consist of pure magnesium and a secondary $Ca_2Mg_6Zn_3$ phase having a hexagonal crystal lattice (Fig. 3,*a*). Ultrasonic treatment and ND doping influenced the matrix and secondary phase distribution in the melt. The lowes fraction of $Ca_2Mg_6Zn_3$ is seen to be in alloy #2. Note there are the redistributed intensities of reflections from the (002) and (110) planes belonging to the matrix phase in alloy #1 with the preferred orientation of <100> compared to those in alloys #2 and #3. The lattice parameter *a*, the unit cell volume *V*, and the *c*/*a* ratio of the matrix phase decrease after ultrasonic treatment and increase after ND doping, as summarized in Table 2.

Microstructural studies made by the SEM instrument in combination with X-ray spectral microanalysis allowed us to identify both the matrix and secondary phases that segregated along the grain boundaries (Fig. 4). The average grain size is seen to vary from 40 μm to 42 μm for all alloys (Fig. 4). Both ultrasonic treatment and ND doping do not contribute significantly to microstructural changes. ND doping reduced the maximum grain size from 153 μm to 135 μm, whereas the average grain size decreased from 41.5 μm to 40 μm for alloys #1 and #3. Visually, according to SEM micrographs and X-ray structural analysis,

Table 1
Chemical composition of the studied alloys, wt.%.

Alloy	Mg	Zn	Ca	Si	Al	Fe
#1 Mg–4Zn–1Ca	94.7 ± 0.06	4.0 ± 0.07	1.0 ± 0.02	0.12 ± 0.01	0.04 ± 0.05	0.03 ± 0.01
#2 (Mg–4Zn–1Ca)$_{US}$	94.4 ± 0.04	4.22 ± 0.08	0.96 ± 0.03	0.16 ± 0.03	0.1 ± 0.02	0.04 ± 0.02
#3 (Mg–4Zn–1Ca)$_{ND}$	93.6 ± 0.05	4.7 ± 0.07	1.3 ± 0.04	0.17 ± 0.04	0.02 ± 0.01	0.02 ± 0.01

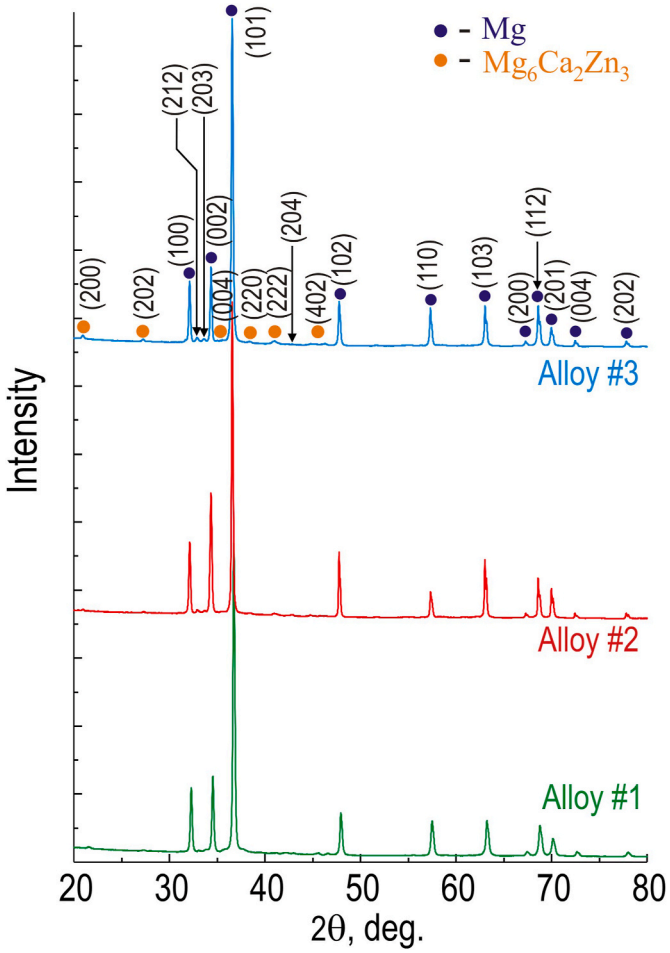

Fig. 3. X-ray diffraction patterns of the studied alloys.

nanodiamond particles were not identified, which is inferential evidence of missing ND large agglomerations.

The specific area occupied by the matrix and secondary phase was analyzed and tabulated for all alloys using the ImageJ software (Table 3). The $Ca_2Mg_6Zn_3$ phase is red-marked in SEM micrographs. The matrix phase predominates, occupying the area from 91.76% to 96.26%, whereas the secondary phase area ranges from 3.74% to 8.24%. In alloy #2, the secondary phase occupies a fewest area.

Element maps depicted in Fig. 5 show the presence of Ca, Zn, and Mg distributed along the grain boundaries. The EDS analysis confirms that the calculated composition is very similar to that detected in the samples (Table 4). The composition of grains represents a solid solution of zinc in magnesium, including areas of pure magnesium, whereas the phase traced along the grain boundaries can be regarded as $Ca_2Mg_6Zn_3$ (Table 5). Calcium turns out to be not contained in the matrix phase since it was detected only in the secondary phase segregated along the grain boundaries. The Zn content in the matrix phase decreases from 1.49 at.% to 0.63 at.%, which accords well with its increase in the secondary phase. Above, the latter's area was found to increase from 3.74% to 8.24% (see Table 3).

Table 2
Data received from X-ray diffraction analysis.

Phase	Volume fraction, %	lattice parameter (Å) and unit cell volume (Å^3)	CSR, nm	Lattice distortion, $\Delta d/d$
Alloy #1 (Mg–Ca–Zn)				
Mg	94	$a = 3.2081$, $c = 5.2117$, $V = 46.4522$, $c/a = 1.6245$	60	$1.5 \cdot 10^{-3}$
$Mg_6Ca_2Zn_3$	6	$a = 10.0236$, $c = 9.6067$, $V = 835.8961$, $c/a = 0.9584$	40	$1.4 \cdot 10^{-3}$
Alloy #2 (Mg–4Zn–1Ca)$_{US}$				
Mg	97	$a = 3.2061$, $c = 5.1731$, $V = 46.0503$, $c/a = 1.6135$	51	$2.3 \cdot 10^{-3}$
$Mg_6Ca_2Zn_3$	3	$a = 10.3415$, $c = 9.6764$, $V = 896.2136$, $c/a = 0.9357$	50	$1.6 \cdot 10^{-3}$
Alloy #3 (Mg–4Zn–1Ca)$_{ND}$				
Mg	93	$a = 3.2090$, $c = 5.2101$, $V = 46.4639$, $c/a = 1.6236$	49	$1.8 \cdot 10^{-3}$
$Mg_6Ca_2Zn_3$	7	$a = 10.3213$, $c = 9.3373$, $V = 861.4315$, $c/a = 0.9047$	53	$1.0 \cdot 10^{-3}$

To assess the biodegradation performance, the samples were tested in vitro under conditions similar to aseptic inflammation. The starting and final masses of the samples after a week's in vitro test are summarized in Table 6. Analyzing the results obtained, we can note that all the samples have a decrease in mass by 6–7% in seven days, except alloy #2. The mass loss in this sample is 18.3 and 23 times less than that in alloys #1 and #3, respectively. Comparatively, the volume fraction of the $Ca_2Mg_6Zn_3$ phase along the grain boundaries in alloy #2 is twice as less than in alloy #1 and #3. In this context, a correlation between the volume fraction of the secondary phase and the mass loss during in vitro testing is obvious. The rationale for the tangled behavior and noted correlation is believed to stem from the nature of the biodegradation of Mg-based alloys, and this phenomenon requires much more examination.

According to AFM data, alloy #2 has the smoothest topography than other alloys. There is slight roughness ranging from 0.01 μm to 0.03 μm (Fig. 6,*d-f*), including solitary prominences up to 0.44 μm.

It's evident that the baseline alloy contains more inclusions up to 0.24 μm in size, while an average size varies from 0.02 μm to 0.1 μm (Fig. 6,*a-c*). The surface topology in alloy #3 turned out to be qualitatively comparable to that found in alloy #1 (Fig. 6,*g-i*). Nevertheless, alloy #3 indicates a more homogeneous structure, which can be addressed to a uniform ND distribution.

Biodegradation of Mg-based is associated with electrochemical processes evolved in an electrically conductive environment contacting with the surface and is triggered by the electrode potential difference between the matrix and secondary phase(s), in our case, $Ca_2Mg_6Zn_3$. The AFM study shows that the surface potential of the matrix phase is equal to an average value of +1.95v, which is higher than that measured for the secondary phase, which is +1.75v (Fig. 7). That being the case, the matrix phase oxidizes much faster than $Ca_2Mg_6Zn_3$. Definitely, the less area occupied by the $Ca_2Mg_6Zn_3$ phase in alloy #2 may result in a slow biodegradation rate. Notably, the maximum surface potential of alloy

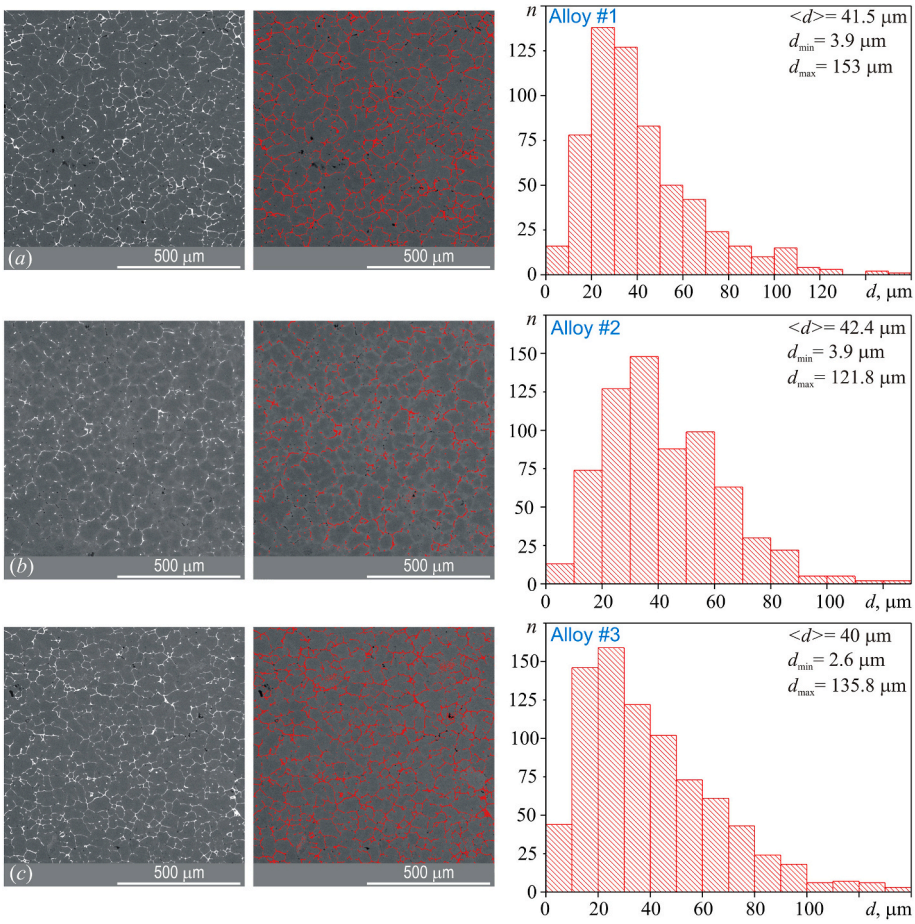

Fig. 4. SEM micrographs and grain size distribution in the studied alloys: #1 (*a*), #2 (*b*), and #3 (*c*).

Table 3
Specific area calculated by the ImageJ software, %.

Alloy	Matrix phase (Mg)	Secondary phase ($Ca_2Mg_6Zn_3$)
#1 (Mg–4Zn–1Ca)	92.94	7.06
#2 $(Mg–4Zn–1Ca)_{US}$	96.26	3.74
#3 $(Mg–4Zn–1Ca)_{ND}$	91.76	8.24

#2 turned out to be around +2.1v, which is much higher than that recorded in alloy #1 (+0.75v) and #3 (+1.27v), respectively. In the AFM study, alloy #2 has the smallest surface roughness; next is alloy #1, and alloy #3 is slightly less pronounced in terms of roughness (see Fig. 6). It is important to point out that the associated biodegradation rate increases from 0.3% to 7.6% in 168 h in the same sequence.

4. Discussion

To comprehensively understand biodegradation processes evolving in vivo, we need to consider the typical chemical reactions that occur during the microgalvanic corrosion of Mg-based alloys in a biological environment. Upon contact with body fluids, Mg oxidizes to metal cations under the anodic reaction described by expression (1). Free electrons are consumed by the cathodic reaction through electrochemical water splitting, according to expression (2). These redox reactions occur randomly over the entire surface where the galvanic bond occurs due to the different potentials arising between the metal matrix and intermetallic/secondary phases or grain boundaries. The bio-environment is very aggressive. Even though magnesium is concealed with a passivating film, consisting mainly of $Mg(OH)_n$, as expression (3) says, due to the high content of chloride ions in the bioactive medium, the protective layer can be demolished with the appearance of pitting corrosion foci.

$M \rightarrow M\,n+ + n\bar{e}$ – anodic reaction (1)

$2H2O + 2\bar{e} \rightarrow H2 + 2OH$ – – cathodic reaction (2)

$M\,2{+}{+}nOH \rightarrow M(OH)n$ – passivating film formation (3)

According to its chemical composition, the RPMI-1640 synthetic culture medium contains the following cations Ca^{2+}, Mg^{2+}, Zn^{2+}, K^+, Na^+, and anions NO_3^-, SO_4^{2-}, $P_2O_7^{4-}$, Cl^-, resulting from the potential electrochemical reactions. Therefore, the following complementary reactions can be expected, which were reported by Li et al. [36]:

$$Mg + H_2O \rightarrow Mg(OH)_2\downarrow + H_2\uparrow \; Mg^{2+} + CO_3^{2-} \rightarrow MgCO_3\downarrow$$

$$Mg(OH)_2 + Cl^- \rightarrow MgCl_2 + OH^- \; H_2PO_4^- \,/\, H_2PO_4^{2-} + OH^- \rightarrow PO_4^{3-} + H_2O$$

$$OH^- + HCO_3 \rightarrow CO_3^{2-} + H_2O \; Mg^{2+} + PO_4^{3-} \rightarrow Mg_3(PO_4)_2\downarrow$$

$$Ca^{2+} + CO_3^{2-} \rightarrow CaCO_3\downarrow \; Ca^{2+} + PO_4^{3-} \rightarrow Ca(PO_4)_2\downarrow$$

The spectrum of electrochemical reactions indicates an intricate process of Mg biocorrosion as a system where very little is controllable, which means that the volume fraction of the $Ca_2Mg_6Zn_3$ phase, in this context, plays a pivotal role in promoting the biodegradation rate. Secondary phases segregated along the grain boundaries form extra galvanic pairs, facilitating the biocorrosion reaction [20,37]. Besides, the length of the grain boundaries affects biodegradation. ND doping leads to as many crystallization nuclei. The latter, in turn, obviously produce grains of smaller size, whereas the grain boundaries seem to

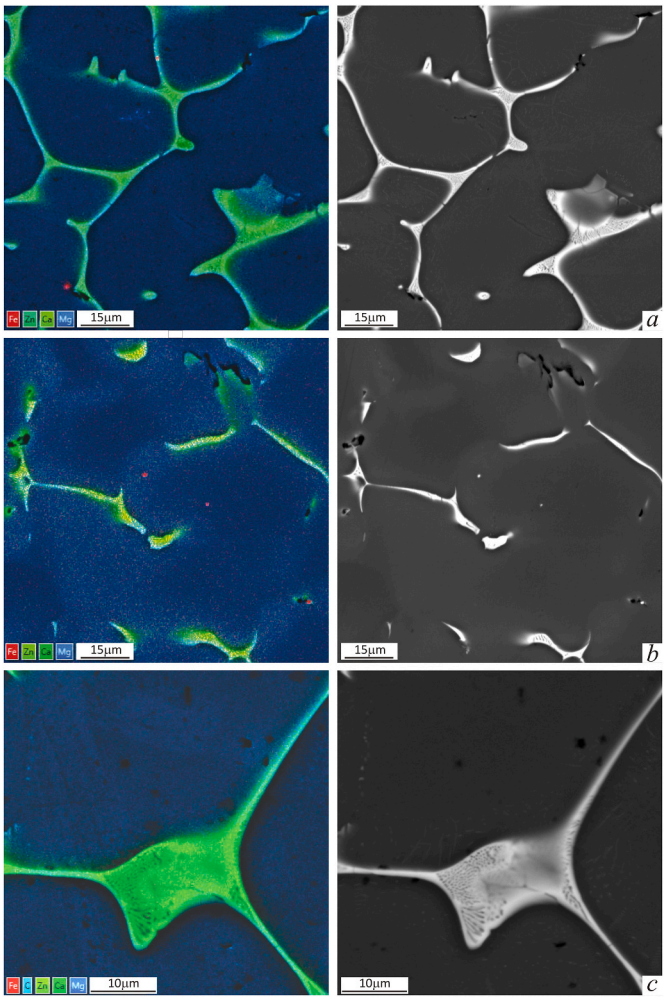

Fig. 5. Element distribution maps and SEM images of the studied alloys: #1 (*a*), #2 (*b*), and #3 (*c*).

Table 4
EDS analysis data on the studied alloys, at.%.

Alloy	Mg	Ca	Zn	Total, at. %
#1 (Mg–4Zn–1Ca)	96.98	0.87	2.14	100
#2 (Mg–4Zn–1Ca)$_{US}$	97.31	0.89	1.8	100
#3 (Mg–4Zn–1Ca)$_{ND}$	96.7	1.03	2.27	100

Table 5
Elementary analysis of the matrix (Mg) and secondary ($Ca_2Mg_6Zn_3$) phase in the alloys, at.%.

Alloy	Mg	Ca	Zn	Total
Matrix phase				
#1 (Mg–4Zn–1Ca)	99.042	0	0.958	100
#2 (Mg–4Zn–1Ca)$_{US}$	98.51	0	1.49	100
#3 (Mg–4Zn–1Ca)$_{ND}$	99.37	0	0.63	100
Secondary phase				
#1 (Mg–4Zn–1Ca)	75.44	8.87	15.69	100
#2 (Mg–4Zn–1Ca)$_{US}$	73.34	6.455	20.21	100
#3 (Mg–4Zn–1Ca)$_{ND}$	71.34	9.21	19.45	100

have become much longer. From Table 6, the corrosion rate in vitro expressed in terms of g/h stands at 0.074/168 and 0.081/168 for alloy #1 and #3, respectively, showing a rise of almost 10%.

Comparing the AFM images related to the surface potential and surface topology measured in alloy #3 provides a sufficiently clear understanding that the electrochemical corrosion reaction is influenced by both the number of galvanic pairs and, as a subsidiary factor, the surface roughness. In addressing the AFM images depicted in Figs. 6 and 7, one may trace the phase along the grain boundary and intrinsic acicular inclusions allocated in the matrix phase. The authors suggest that the larger the specific rough surface, the more phases can interact with electrolytes, resulting in faster decomposition.

Considering alloy #2, the ultrasonic treatment of the baseline Mg–4Zn–1Ca alloy' melt has a beneficial effect on expected biodegradation. The lower volume fraction of the secondary $Ca_2Mg_6Zn_3$ phase decreased from 6% to 3% therein, leading to the biodegradation term having increased 18.5-fold. The findings correlate well with the data reported by other researchers, where the rationale of inhibited decomposition performance in Mg-xZn-1Ca alloys is also ascribed to the secondary phase(s) formed during the melt solidification process [38–42]. The corrosion rate increases due to the diverse electrochemical behavior shown by the α-Mg (cathode) and secondary (anode) phases [39]. The cathode/anode ratio, in terms of the specific area, affects the corrosion rate in Mg-based alloys; i.e., a larger area ratio contributes to faster corrosion [41,42]. Zn addition up to 3 wt% in the Mg–1Ca alloy is known to improve corrosion resistance due to a decreased volume fraction of the secondary Mg_2Ca phase [42]. The latter is an intermediate product in the synthesis of $Ca_2Mg_6Zn_3$; therefore, this secondary phase in the galvanic system is considered the anode. Since the pitted surface is highly corrosion-prone, homogenization annealing with subsequent quenching was reported to enhance the corrosion resistance in the Mg–6Al–1Zn–2Ca and Mg–6Al–1Zn alloy due to improved superficial microstructure containing micro-pits in lesser quantities [40]. As for other alloys, e.g., Mg–6Al–1Zn subjected to heat treatment and holding at 693K for 48 h, β-phases dissolve in the matrix, reducing the number of pitting corrosion foci and, consequently, a number of galvanic cathodes [39,43].

The next crucial factor affecting biodegradation performance is the surface state. Our work demonstrates that the less pronounced surface roughness, the lower the biodegradation rate. Thus, alloy #2, which melt was ultrasonically homogenized with subsequent heat treatment at 300 °C for 6 h, has both the smoothest surface and the lowest biodegradation rate compared to those related to alloy #1 and #3 after the same heat treatment. Exploring the surface topology of the Mg–6Al–1Zn–2Ca and Mg–6Al–1Zn alloy using an SEM instrument equipped with an electron probe microanalyzer sheds more light on this issue [39]. The authors reasonably concluded that the less the arithmetic mean between the minimum and maximum roughness, the lower the biodegradation rate, which is consistent with our findings. One of the implicit objectives of our study was to evaluate whether ND doping the melt extends the grain boundaries and how much this affects the biodegradation rate. However, no remarkable changes were noted. Besides, ND doping is known to increase the ultimate strength due to finely dispersed hardening [44].

Combining data published in the literature and our findings, the authors consider alloy #2-based biomaterials among the most promising directions for further applied studies if a longer biodegradation term is presumed. In addition to maintaining the virtue of the encouraging results, alloy #3, where the melt might be ultrasonically treated and subsequently homogenized for dissolution of secondary phases in the Mg matrix, deserves special attention for further exploration and clinical applications.

5. Conclusions

In summary, this study demonstrates that modifications applied to the baseline Mg–4Zn–1Ca-based alloy affect both the matrix and surface, which is of crucial importance in view of the increasing requirements for higher-level biodegradable implants. Based on the data obtained, the following conclusions have been formulated:

Table 6
Sample mass before and after in vitro biodegradation in the RPMI-1640 medium.

Alloy	Starting mass (M1), mg	After a week in vitro biodegradation test		
		*Dry weight (M2), mg	Weight decrement (M3), mg	Weight decrement (M4), % of M1
#1 (Mg–4Zn–1Ca)	1.225	1.151	0.074	6.0408
#2 (Mg–4Zn–1Ca)$_{US}$	1.213	1.209	0.004	0.3298
#3 (Mg–4Zn–1Ca)$_{ND}$	1.068	0.987	0.081	7.5843

Note: *M2 – sample mass after one-week biotesting and subsequent two-week drying in the air.

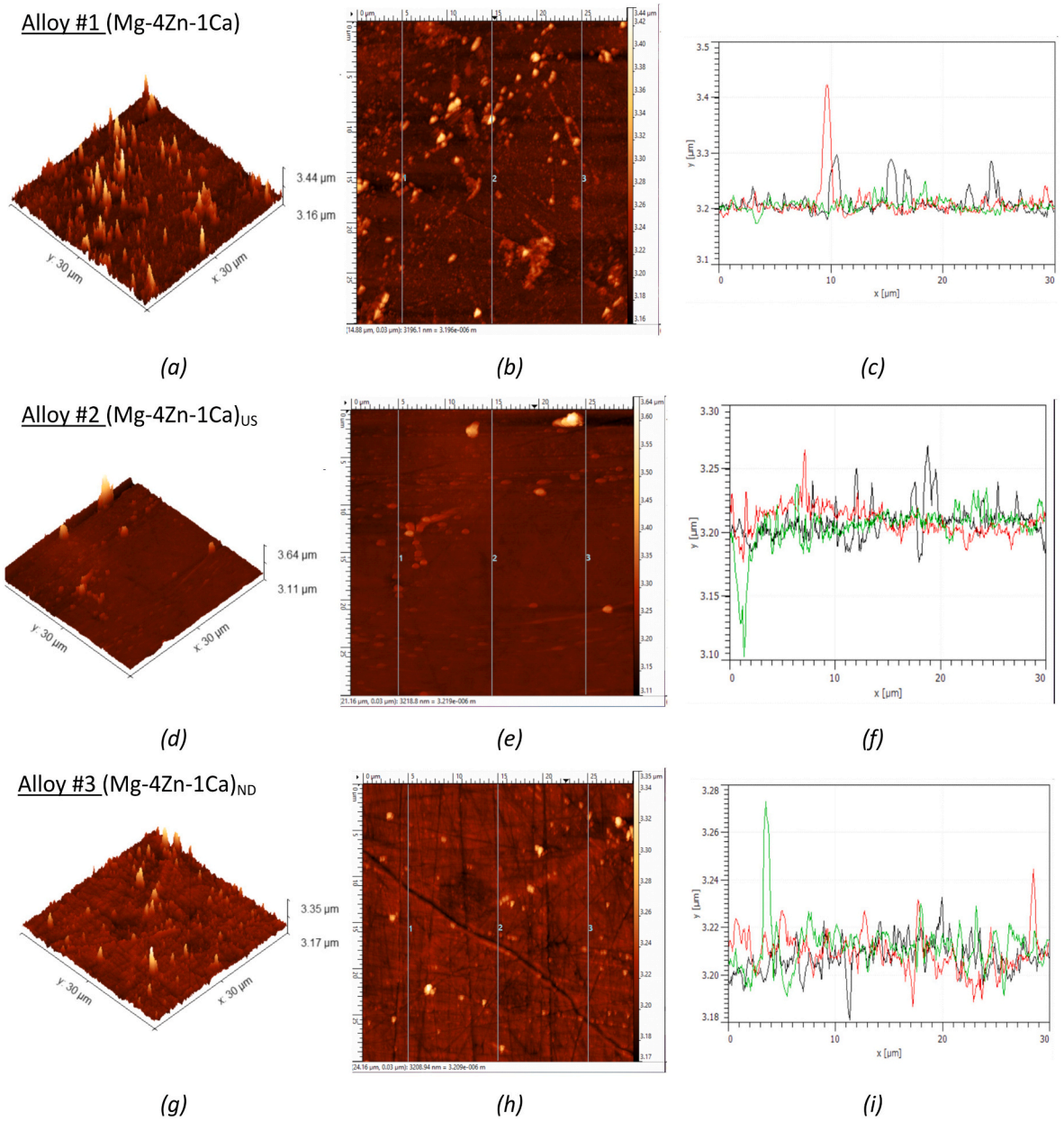

Fig. 6. AFM 3-D (*a, d, g*) and 2-D (*b, e, h*) topographic images and profile of phase inclusions (*c, f, i*) traced along the vertical lines marked in 2-D images.

1. X-ray diffraction analysis showed that all the studied alloys consist of the matrix (Mg) and secondary ($Ca_2Mg_6Zn_3$) phase. Ultrasonic treatment and ND doping affected the redistribution of the matrix and secondary phase in the alloy #2 melt, where the fewest volume fraction of the secondary phase was detected;
2. Structural analysis testifies that US treatment and ND doping have negligible effects on the microstructural features. The average grain size varies from 40 µm to 42 µm in all the studied alloys.
3. There is a correlation between the volume fraction of the $Ca_2Mg_6Zn_3$ phase segregated along the grain boundaries and the mass loss during in vitro tests using the RPMI-1640 synthetic culture medium. The fewer this fraction, the lower the biodegradation rate.
4. US treatment appears to retard the decomposition rate. Namely, the latter measured in alloy #2 is almost 20 times slower than that in others. The in vitro study revealed that the mass of sample #2 decreased by 0.3298%. The rationale for the inhibited

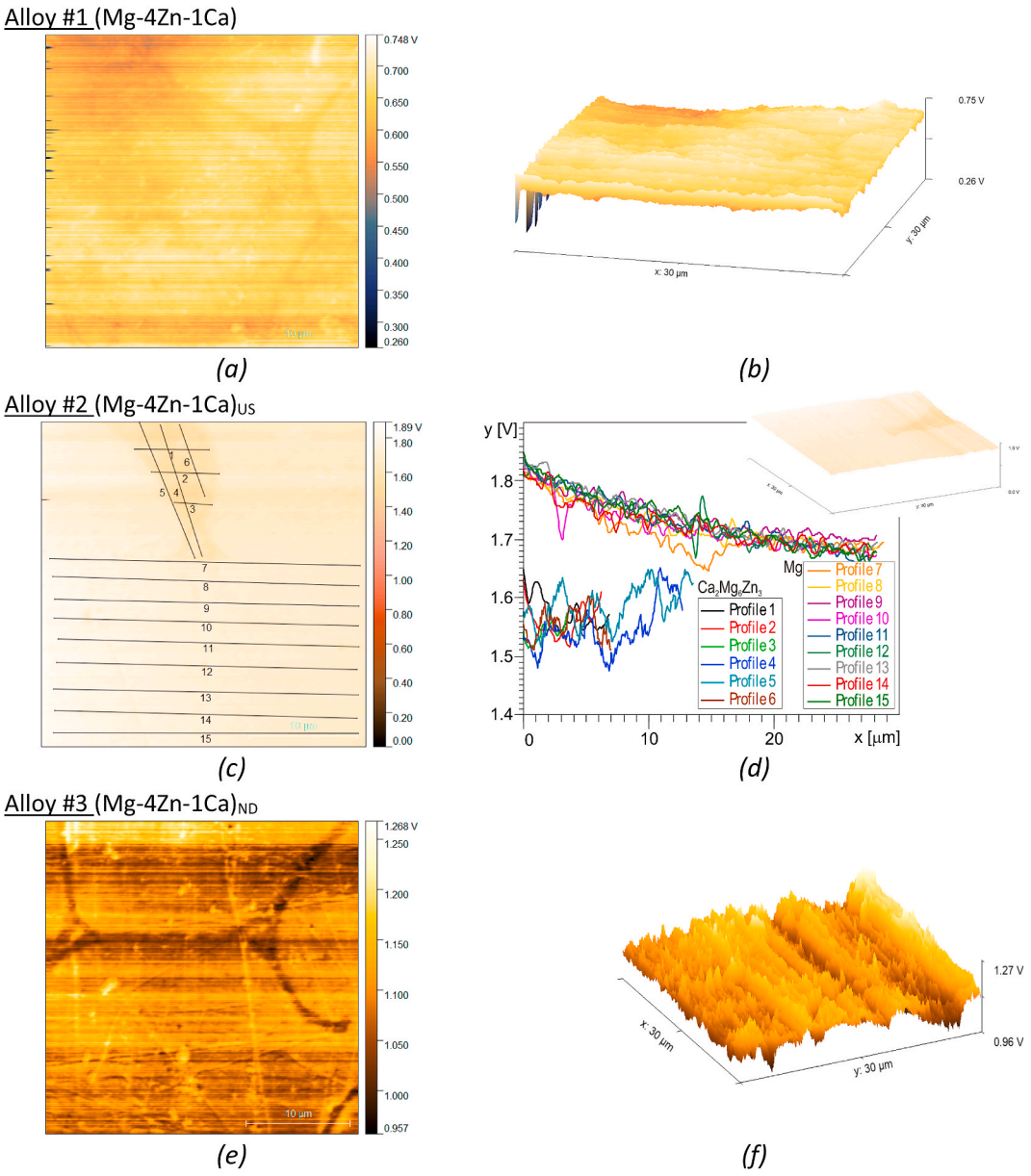

Fig. 7. AFM 2-D (*a, c, e*) and 3-D (*b, f*) images of the surface potential distribution; detailed values of the surface potential measured for the $Ca_2Mg_6Zn_3$ (1–6) and matrix (7–15) phase in alloy #2 (*d*).

biodegradation performance is the reduced specific area occupied by the secondary $Ca_2Mg_6Zn_3$ phase along the grain boundaries

5. ND doping does not remarkably affect the biodegradation rate. However, biodegradation turned out to be facilitated by surface roughness; the higher the latter, the faster the electrochemical corrosion reaction. Alloy #2 indicated the smoothest surface.

CRediT authorship contribution statement

Ekaterina Marchenko: Conceptualization, Methodology, Project administration, Supervision, Funding acquisition. **Gulsharat Baigonakova:** Investigation, Formal analysis, Visualization, Writing – original draft. **Anton Khrustalev:** Investigation, Formal analysis, Visualization, Writing – original draft, Writing – review & editing. **Ilya Zhukov:** Investigation, Formal analysis, Visualization. **Aleksandr Vorozhtsov:** Conceptualization, Methodology, Supervision, Funding acquisition. **Timofey Chekalkin:** Investigation, Formal analysis, Visualization, Writing – original draft, Writing – review & editing. **Aleksandr Monogenov:** Software, Validation. **Aleksandr Garin:** Software, Validation. **Seung-Baik Kang:** Conceptualization, Methodology, Writing – review & editing, Supervision, Funding acquisition. **Tae-Woo Kim:** Investigation, Formal analysis, Visualization, All authors made substantive edits for critical content and approved the final manuscript.

Funding

This work was carried out with financial support from the Q2 Ministry of Science and Higher Education of the Russian Federation (agreement no. 075-15-2021-1384) and Bio & Medical Technology Development Program of the National Research Foundation (NRF) funded by the Korean government (2021K1A3A1A49098116)

Declaration of competing interest

The authors declare that they have no known competing financial interests or personal relationships that could have appeared to influence

the work reported in this paper.

Data availability

Data will be made available on request.

Acknowledgment

This work was carried out with financial support from the Ministry of Science and Higher Education of the Russian Federation (agreement no. 075-15-2021-1384).

References

[1] H.S. Han, S. Loffredo, I. Jun, et al., Current status and outlook on the clinical translation of biodegradable metals, Mater. Today 23 (2019) 57–71, https://doi.org/10.1016/j.mattod.2018.05.018.
[2] Y.J. Ren, J.J. Huang, K. Yang, et al., Study of bio-corrosion of pure magnesium, Acta Metall. Sin. 41 (2005) 1228. https://www.ams.org.cn/EN/Y2005/V41/I11/1228.
[3] Z.G. Huan, M.A. Leeflang, L.E. Fratila-Apachitei, et al., In vitro degradation behavior and cytocompatibility of Mg–Zn–Zr alloys, J. Mater. Sci. Mater. Med. 21 (2010) 2623–2635, https://doi.org/10.1007/s10856-010-4111-8.
[4] M. Razavi, M. Fathi, O. Savabi O, et al., Biodegradable magnesium bone implants coated with a novel bioceramic nanocomposite, Materials 13 (2020) 1315, https://doi.org/10.3390/ma13061315.
[5] X. Wang, L.H. Dong, J.T. Li, et al., Microstructure, mechanical property and corrosion behavior of interpenetrating (GA + β-TCP)/MgCa composite fabricated by suction casting, Mater. Sci. Eng. C 33 (2013) 4266, https://doi.org/10.1016/j.msec.2013.06.018.
[6] R.B. Heimann, Magnesium alloys for biomedical application: advanced corrosion control through surface coating, Surf. Coat. Technol. 405 (2021), 126521, https://doi.org/10.1016/j.surfcoat.2020.126521.
[7] Y. Liu, Y. Zhang, Y.L. Wang, et al., Research progress on surface protective coatings of biomedical degradable magnesium alloys, J. Alloys Compd. 885 (2021), 161001, https://doi.org/10.1016/j.jallcom.2021.161001.
[8] R. Kumar, P. Katyal, Effects of alloying elements on performance of biodegradable magnesium alloy, Mater. Today Proc. 56 (2022) 2443–2450, https://doi.org/10.1016/j.matpr.2021.08.233.
[9] C. Gao, S. Li, L. Liu, et al., Dual alloying improves the corrosion resistance of biodegradable Mg alloys prepared by selective laser melting, J. Magnes. Alloy. 9 (2021) 305–316, https://doi.org/10.1016/j.jma.2020.03.016.
[10] X. Li, X. Liu, S. Wu, et al., Design of magnesium alloys with controllable degradation for biomedical implants: from bulk to surface, Acta Biomater. 45 (2016) 2–30, https://doi.org/10.1016/j.actbio.2016.09.005.
[11] F. Witte, The history of biodegradable magnesium implants: a review, Acta Biomater. 6 (2010) 1680–1692, https://doi.org/10.1016/j.actbio.2010.02.028.
[12] F. Witte, F. Feyerabend, P. Maier, et al., Biodegradable magnesium-hydroxyapatite metal matrix composites, Biomaterials 28 (2007) 2163–2174, https://doi.org/10.1016/j.biomaterials.2006.12.027.
[13] M. Razavi, M. Phathi, O. Savabi, et al., Biodegradable magnesium alloy coated by fluoridated hydroxyapatite using MAO/EPD technique, Surf. Eng. 30 (2014) 545–551, https://doi.org/10.1179/1743294414Y.0000000284.
[14] Y.F. Zheng, X.N. Gu, F. Witte, Biodegradable metals, Mater. Sci. Eng. R. 77 (2014) 1–34, https://doi.org/10.1016/j.mser.2014.01.001.
[15] K. Kusnierczyk, M. Basista, Recent advances in research on magnesium alloys and magnesium-calcium phosphate composites as biodegradable implant materials, J. Biomater. Appl. 31 (2017) 878–900, https://doi.org/10.1177/0885328216657271.
[16] M.P. Staiger, A.M. Pietak, J. Huadmai, G. Dias, Magnesium and its alloys as orthopedic biomaterials: a review, Biomaterials 27 (2006) 1728–1734, https://doi.org/10.1016/j.biomaterials.2005.10.003.
[17] M. Niinomi, Recent metallic materials for biomedical applications, Metall. Mater. Trans. A 33 (2002) 477, https://doi.org/10.1007/s11661-002-0109-2.
[18] S. Zhang, X. Zhang, C. Zhao, et al., Research on an Mg-Zn alloy as a degradable biomaterial, Acta Biomater. 6 (2010) 626–640, https://doi.org/10.1016/j.actbio.2009.06.028.
[19] R.Y. Liu, R.G. He, L.Q. Xu, S.F. Guo, Design of Fe-Mn-Ag alloys as potential candidates for biodegradable metals, Acta Metall. Sin. 31 (2019) 584–590, https://doi.org/10.1007/s40195-018-0702-z.
[20] I.J. Polmear, Light Alloys: from Traditional Alloys to Nanocrystals//, Butterworth-Heinemann, Elsevier, Oxford, 2006, p. 237.
[21] J.Z. Ilich, J.E. Kerstetter, Nutrition in bone health revisited: a story beyond calcium, J. Am. Coll. Nutr. 19 (2000) 715–737, https://doi.org/10.1080/07315724.2000.10718070.
[22] Z.J. Li, X.N. Gu, S.Q. Lou, Y.F. Zheng, The development to binary Mg–Ca alloys for use as biodegradable materials within bone, Biomaterials 29 (2008) 1329–1344, https://doi.org/10.1016/j.biomaterials.2007.12.021.
[23] Y.C. Li, M.H. Li, W.Y. Hu, et al., Biodegradable Mg-Ca and Mg-Ca-Y alloys for regenerative medicine, Mater. Sci. Forum 654–656 (2010) 2192. https://doi.org/10.4028/www.scientific.net/MSF.654-656.2192. –95.
[24] H.R. Bakhsheshi-Rad, M.H. Idris, M.R. Abdul-Kadir, et al., Mechanical and bio-corrosion properties of quaternary Mg–Ca–Mn–Zn alloys compared with binary Mg–Ca alloys, Mater. Des. 53 (2014) 283–292, https://doi.org/10.1016/j.matdes.2013.06.055.
[25] H. Dieringa, N. Hort. Magnesium-based metal matrix nanocomposites-processing and properties. In: & Materials Society, T. (eds) TMS 2018 147th Annual Meeting & Exhibition Supplemental Proceedings. TMS 2018. The Minerals, Metals & Materials Series. Springer, Cham. 679–691. https://doi.org/10.1007/978-3-319-72526-0_64.
[26] A. Khrustalyov, A. Kozulin, I. Zhukov, et al., Influence of titanium diboride particle size on structure and mechanical properties of an Al-Mg alloy, Metals 9 (2019) 1030, https://doi.org/10.3390/met9101030.
[27] M. Malaki, W. Xu, A.K. Kasar, et al., Advanced metal matrix nanocomposites, Metals 9 (2019) 330, https://doi.org/10.3390/met9030330.
[28] Y. Watanabe, T. Sugiura, H. Sato, et al., Fabrication of Al-based composites by centrifugal mixed-powder method and their application for grinding wheels, J. Mater. Eng. Perform. 28 (2019) 3852–3863, https://doi.org/10.1007/s11665-019-03917-3.
[29] H. Gong, B. Anasori, C.R. Dennison, et al., Fabrication, biodegradation behavior and cytotoxicity of Mg-nanodiamond composites for implant application, J. Mater. Sci. Mater. Med. 26 (2015) 110, https://doi.org/10.1007/s10856-015-5441-3.
[30] B. Zhang, Y. Hou, X. Wang, et al., Mechanical properties, degradation performance and cytotoxicity of Mg-Zn-Ca biomedical alloys with different compositions, Mater. Sci. Eng., C 31 (2011) 1667–1673, https://doi.org/10.1016/j.msec.2011.07.015.
[31] Z.G. Xu, C. Smith, S.O. Chen, J. Sankar, Development and microstructural characterizations of Mg-Zn-Ca alloys for biomedical applications, Mater. Sci. Eng. B 176 (2011) 1660–1665, https://doi.org/10.1016/j.mseb.2011.06.008.
[32] C. Liu, X. Chen, J. Chen, et al., The effects of Ca and Mn on the microstructure, texture and mechanical properties of Mg-4 Zn alloy, J. Magnes. Alloy. 3 (2021) 1084–1097, https://doi.org/10.1016/j.jma.2020.03.012.
[33] S. Vorozhtsov, L. Minkov, V. Dammer, et al., Ex situ introduction and distribution of nonmetallic particles in aluminum melt: modeling and experiment, J. Occup. Med. 69 (2017) 2653–2657, https://doi.org/10.1007/s11837-017-2594-1.
[34] B. Zeka, B. Markoli, P. Mrvar, et al., Suitability of moulding materials for Al-Li alloy casting, Mater. Technol. 55 (2021) 311–316, https://doi.org/10.17222/mit.2020.208.
[35] S. Vorozhtsov, A. Vorozhtsov, O. Kudryashova, et al., Structural and mechanical properties of aluminium-based composites processed by explosive compaction, Powder Technol. 313 (2017) 251–259, https://doi.org/10.1016/j.powtec.2017.03.027.
[36] Y. Li, Q. Li, H. Wang, et al., Recent progresses in oxygen reduction reaction electrocatalysts for electrochemical energy applications, Electrochem. Energ. Rev. 2 (2019) 518–538, https://doi.org/10.1007/s41918-019-00052-4.
[37] M.M. Avedesian, H. Baker, ASM Specialty Handbook: Magnesium and Magnesium Alloys, ASM international, 1999, p. 17.
[38] E. Dabah, G. Ben-Hamu, V. Lisitsyn, et al., The influence of Ca on the corrosion behavior of new die cast Mg–Al-based alloys for elevated temperature applications, J. Mater. Sci. 45 (2010), 300715, https://doi.org/10.1007/s10853-010-4302-1.
[39] S. Mathieu, C. Rapin, J. Steinmetz, P. Steinmetz, A corrosion study of the main constituent phases of AZ91 magnesium alloys, Corrosion Sci. 45 (2003), 274155, https://doi.org/10.1016/S0010-938X(03)00109-4.
[40] R.K. Singh Raman, The role of microstructure in localized corrosion of magnesium alloys, Metall. Mater. Trans. 35 (2004), 252531, https://doi.org/10.1007/s11661-006-0233-5.
[41] M.C. Zhao, M. Liu, G. Song, A. Atrens, Influence of the β-phase morphology on the corrosion of the Mg alloy AZ91, Corrosion Sci. 50 (2008), 193953, https://doi.org/10.1016/j.corsci.2008.04.010.
[42] M. Yuasa, X. Huang, K. Suzuki, et al., Effects of solution treatment on corrosion properties of Mg–6 mass%Al–1 mass%Zn–2 mass%Ca (AZX612) and Mg–6 mass% Al–1 mass%Zn (AZ61) alloys, Mater. Trans. 59 (2018) 1173–1179, https://doi.org/10.2320/matertrans.M2018085.
[43] G. Song, A.L. Bowles, D.H. StJohn, Corrosion resistance of aged die cast magnesium alloy AZ91D, Mater. Sci. Eng. 366 (2004) 7486, https://doi.org/10.1016/j.msea.2003.08.060.
[44] A. Rehman, S. Houshyar, X. Wang, Nanodiamond-based fibrous composites: a review of fabrication methods, properties, and applications, ACS Appl. Nano Mater. 4 (2021) 2317–2332, https://doi.org/10.1021/acsanm.1c00470.